processes

MDPI

Article

Construction of Honeycomb-like ZnO/g-C_3N_5 Heterojunction for MB Photocatalytic Degradation

Sitong Liu [1,†], Shicheng Liu [2,†], Letao Li [3], Letong Yang [3], Xiaodong Wu [1,3,*], Zhichun Si [4], Rui Ran [1] and Hui Wu [3]

[1] State Key Laboratory of New Ceramic and Fine Processing, School of Materials Science and Engineering, Tsinghua University, Beijing 100084, China; stt9320@tsinghua.edu.cn (S.L.); ranr@tsinghua.edu.cn (R.R.)
[2] School of College of Life and Environmental Science, Minzu University of China, Beijing 100081, China; shichengliu@muc.edu.cn
[3] Key Laboratory of Advanced Materials of Ministry of Education, School of Materials Science and Engineering, Tsinghua University, Beijing 100084, China; llt22@mails.tsinghua.edu.cn (L.L.); ylt22@mails.tsinghua.edu.cn (L.Y.); huiwu@tsinghua.edu.cn (H.W.)
[4] Advanced Materials Institute, Graduate School at Shenzhen, Tsinghua University, Shenzhen 518055, China; si.zhichun@sz.tsinghua.edu.cn
* Correspondence: wuxiaodong@tsinghua.edu.cn
† These authors contributed equally to this work.

Abstract: In this study, a combination of calcination and hydrothermal methods was employed to synthesize a honeycomb-like ZnO/g-C_3N_5 (ZCN) heterojunction in situ. The ZCN heterojunction photocatalyst exhibits remarkable photocatalytic degradation performance, achieving a 97% methyl blue (MB) degradation rate with the rate constant of 0.0433 min^{-1} (almost twice that of ZnO). Optical performance tests reveal that the ZCN heterojunction broadens the absorption edge to 710 nm and enhances the charge carrier separation. The presence of abundant oxygen vacancies, as revealed by X-ray photoelectron spectroscopy analysis, effectively suppresses the recombination of photogenerated electron–hole pairs. Furthermore, density functional theory simulations indicate that the combination of ZnO and g-C_3N_5 creates an internal electric field due to their differing work functions. This leads to the formation of a Z-scheme heterojunction that effectively suppresses charge carrier recombination and preserves the strong redox capabilities of ZnO and g-C_3N_5. Finally, electron spin resonance results indicate that O_2^- and OH are the primary active radicals involved in the degradation process. This study introduces a potential approach for the development of highly efficient Z-scheme photocatalysts for water treatment applications.

Keywords: zinc oxide; g-C_3N_5; Z-scheme heterojunction; simulated sunlight photocatalysis; methyl blue elimination

check for updates

Academic Editor: Izabela Czekaj

Received: 23 December 2024
Revised: 3 January 2025
Accepted: 10 January 2025
Published: 16 January 2025

Citation: Liu, S.; Liu, S.; Li, L.; Yang, L.; Wu, X.; Si, Z.; Ran, R.; Wu, H. Construction of Honeycomb-like ZnO/g-C_3N_5 Heterojunction for MB Photocatalytic Degradation. *Processes* **2025**, *13*, 253. https://doi.org/10.3390/pr13010253

Copyright: © 2025 by the authors. Licensee MDPI, Basel, Switzerland. This article is an open access article distributed under the terms and conditions of the Creative Commons Attribution (CC BY) license (https://creativecommons.org/licenses/by/4.0/).

1. Introduction

Rapid industrialization has substantially resulted in the increased presence of various dyes in water systems [1]. These dye pollutants pose significant risks to human health and environmental sustainability due to their carcinogenic properties and limited biodegradability in the environment [2]. To resolve these problems, various techniques have been employed for water treatment to eliminate organic pollutants, such as membrane separation [3], chemical oxidation [4], coagulation [5], and adsorption [6]. However, these methods are expensive and complex and may even result in the generation of toxic by-products. Hence, it is essential to develop effective techniques to overcome these drawbacks.

In recent years, semiconductor-based photocatalysis has gained attention as a promising and sustainable strategy to tackle this issue. During the photocatalysis process, electron–hole pairs are generated in the conduction band (CB) and valence band (VB) of a semiconductor upon irradiation with simulated sunlight [7]. Subsequently, the electron in the CB reacts with oxygen (O_2) to form superoxide radical anions (O^{2-}), while the hole in the VB interacts with water to produce hydroxyl radicals (OH). These two highly reactive radicals are considered vital species in degrading organic pollutants in water. Various semiconductor photocatalysts such as zinc oxide (ZnO) [8], titanium dioxide (TiO_2) [9], and cadmium sulfide (CdS) [10] have been successfully applied in water purification. Among them, ZnO has emerged as a highly promising material for both solar energy conversion and the photodegradation of organic pollutants, thanks to its low toxicity, abundant availability, excellent chemical and optical stability, superior photocatalytic efficiency, and affordability [11,12]. Yashni et al. synthesized ZnO nanoparticles from *Citrus sinensis* peels to degrade Congo red (CR) under UV irradiation. The results showed that the ZnO/UV system achieved 96.73% CR decolorization and 96.70% COD removal under optimized operation parameters (0.171 g of ZnO nanoparticles, pH 6.43, and 5 $mg{\cdot}L^{-1}$ of CR) [13]. Sahu et al. prepared ZnO, SnO_2, and MoS_2 to degrade dye pollutants like Rhodamine B (RhB) and CR under simulated sunlight irradiation, among which ZnO (88.02% RhB, 76.56% CR) exhibited higher degradation performance than the other two photocatalysts (80.11% RhB and 74.25% CR for SnO_2; 78.63% RhB and 73.14% CR for MoS_2) [14]. However, the following two issues still hinder the practical applicability of ZnO, which urgently needs to be resolved: (i) ZnO primarily responds to ultraviolet light (bandgap of 3.20 eV), resulting in minimal utilization of visible light. (ii) The photoinduced electron–hole pairs in pure ZnO have a short lifetime [15].

Graphite nitride carbon (g-C_3N_5) is considered a novel semiconductor with significant potential in energy and environmental applications, thanks to its stability, eco-friendliness, and responsiveness to visible light irradiation [16]. Moreover, the nitrogen-rich conjugated structure diminishes the barriers for electron transitions and enhances electron mobility, thereby augmenting its potential utility in the photocatalytic degradation of aqueous pollutants [17]. However, g-C_3N_5 is inherently limited by considerable carrier recombination and a lack of sufficient reactive sites, which restricts its photocatalytic efficiency. Many researchers have overcome the above drawbacks via constructing heterojunctions. Guan et al. designed a g-C_3N_5/Ti_3C_2 binary heterojunction to improve the photocatalytic performance of g-C_3N_5 [18]. After coupling with Ti_3C_2, the composite displayed 81.6% antibiotic tetracycline degradation within 60 min, which is much higher than that of g-C_3N_4/Ti_3C_2 (65.3%), Ti_3C_2 (50%), g-C_3N_4 (60.7%), and g-C_3N_5 (33.1%). They believe that the enhanced photoactivity can be attributed to the improvements in the light harvest, the charge carrier separation, and the surface reaction rate caused by constructing the heterojunction with Ti_3C_2. Chen et al. constructed a g-C_3N_5/Bi_2MoO_6 heterojunction for aflatoxin B1 photocatalytic degradation [19]. After coupling Bi_2MoO_6 with g-C_3N_5, the photodegradation efficiency of AFBi was improved to 92% within 75 min. The integration of g-C_3N_5 enhances the separation and migration efficiency of photogenerated carriers in Bi_2MoO_6. It has been reported that a ZnO nanosphere with a large specific surface area and reactive sites will facilitate the transfer and recombination of photogenerated electrons [20]. Therefore, integrating g-C_3N_5 nanosheets with ZnO nanospheres to establish a heterojunction may be an effective strategy to enhance the photocatalytic efficiency of sole ZnO and g-C_3N_5, which is the primary aim of this work.

2. Materials and Methods

2.1. Chemicals and Materials

Zinc nitrate hexahydrate ($Zn(NO_3)_2 \cdot 6H_2O$), trisodium citrate dehydrate ($C_6H_5Na_3O_7 \cdot 2H_2O$), urea ($CH_4N_2O$), 3-Amino-1,2,4-triazole (3-AT), methylene blue (MB), and ethanol (EtOH) were bought from Aladdin Biochemical Technology Co., Ltd., Shanghai, China. 5,5-dimethyl-1-pyrroline nitrogen oxide (DMPO) was bought from Alfa Aesar Chemical Co., Ltd., Tianjin, China. All experimental reagents were used directly without further purification. Deionized (DI) water (18.25 MΩ/cm) was used in the experiments.

2.2. Synthesis of Catalysts

2.2.1. Synthesis of g-C_3N_5

Figure 1a illustrates the synthesis process of bulk carbon nitride (g-C_3N_5). This material was prepared using a modified one-step thermal polymerization method [21]. Specifically, 6 g of 3-AT was placed in a sealed crucible and heated in a muffle furnace. The material was calcined at 550 °C for 4 h, with a heating rate of 5 °C per minute. After cooling, the resulting orange powder was ground and collected as the reference sample.

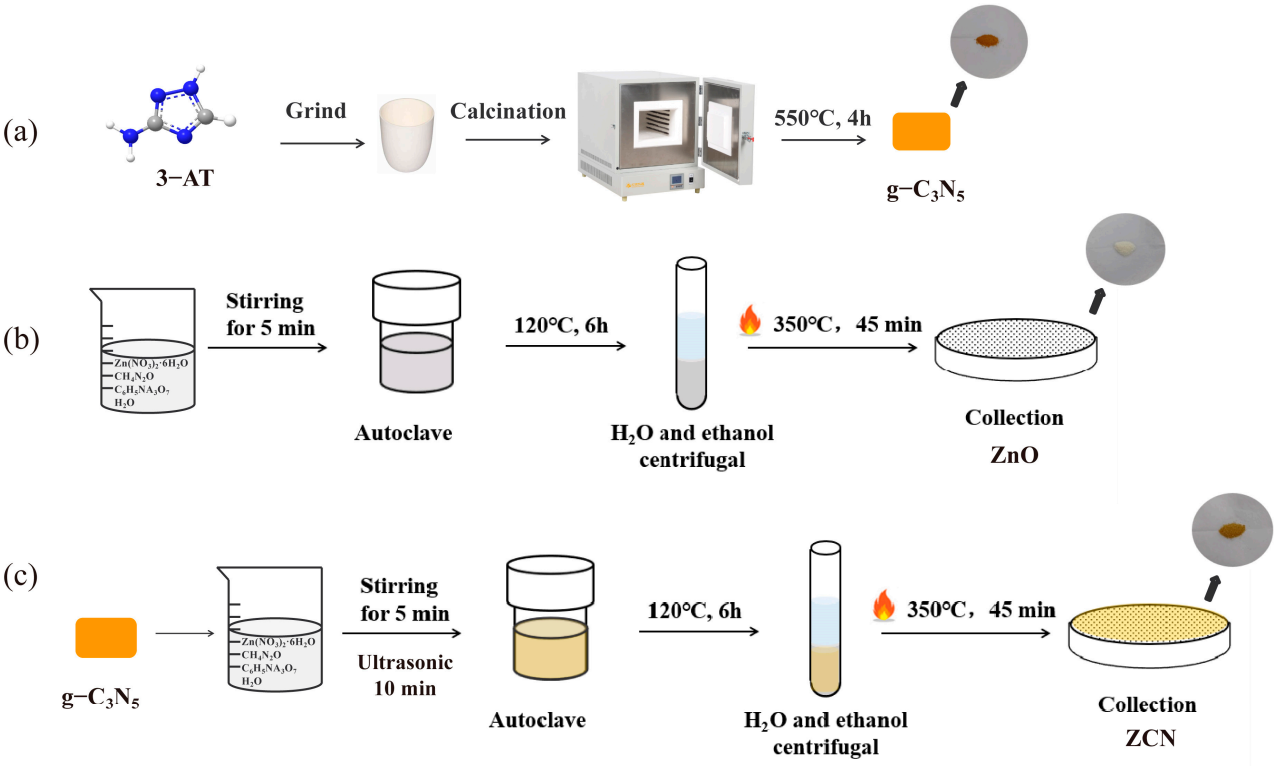

Figure 1. Scheme of the synthesis processes of (**a**) ZnO, (**b**) g-C_3N_5, and (**c**) ZCN samples.

2.2.2. Synthesis of ZnO and ZnO/g-C_3N_5

ZnO was synthesized using an improved hydrothermal method, building on the approach outlined in the literature [22]. The synthesis procedure is as follows (Figure 1b): 0.05 mol of $Zn(NO_3)_2 \cdot 6H_2O$, 0.1 mol of CH_4N_2O, and 0.005 mol of $C_6H_5Na_3O_7 \cdot 2H_2O$ were first dissolved in 75 mL of deionized water. The solution was stirred for 5 min, then transferred to a 100 mL autoclave. It was heated at 120 °C for 6 h to facilitate the reaction. After cooling to room temperature, the resulting product was thoroughly washed three times with deionized water and ethanol. Finally, the material was subjected to annealing at 350 °C for 45 min in a tubular furnace. Then, the white powder was collected as another reference sample. The synthesis process of ZnO/g-C_3N_5 (ZCN) is similar to that of ZnO

except for adding g-C_3N_5 powder at an optimized mass ratio of ZnO/g-C_3N_5 = 1:0.8 in the precursor solution (Figure S1). Finally, the yellow powder was obtained as an experimental sample (Figure 1c).

2.3. Characterization of Samples

X-ray powder diffraction (XRD) patterns were obtained with a D8 advanced X-ray diffractometer (Bruker, Karlsruhe, Germany) equipped with Cu Kα radiation at 40 kV and 40 mA. Fourier transform infrared spectroscopy (FTIR) was performed using a Nicolet iS20 spectrometer (Thermo Fisher Scientific, Waltham, MA, USA) to analyze surface functional groups. Morphological features were examined via field emission scanning electron microscopy (FE-SEM) using a Merlin compact SEM (Zeiss, Oberkochen, Germany). Specific surface areas and pore size distributions were determined through Brunauer-Emmett-Teller (BET) and Barrett-Joyner-Halenda (BJH) methods with a JW-BK200 instrument (JWGB, Beijing, China). The valence states of elements were analyzed by X-ray photoelectron spectroscopy (XPS) using an ESCALAB Xi+ spectrometer (Thermo Fisher Scientific, Waltham, USA). UV-vis diffuse reflectance spectra (UV-vis DRS) in the range of 200–800 nm were recorded with a UV2600 spectrometer (Shimadzu, Kyoto, Japan). Photoluminescence (PL) spectra were measured using an F-7100 fluorescence spectrometer (Hitachi, Tokyo, Japan), and electron spin resonance (ESR) signals were recorded with an A300 spectrometer (Bruker, Karlsruhe, Germany).

2.4. Degradation Experiments

The photocatalytic MB decomposition tests with different catalysts were carried out under the exposure of a 300 W Xe lamp. Typically, the photocatalysts (0.2 g·L^{-1}) were dispersed in the 50 mL MB solution (30 mg·L^{-1}) using ultrasonic treatment, followed by magnetic stirring to reach adsorption-desorption equilibrium. The simulated light source was then turned on to begin the reaction. At 10 min intervals, 6 mL samples were collected, filtered through a 0.22 μm polyether sulfone membrane, and analyzed using a UV-visible spectrophotometer at 664 nm. To ensure reliability and minimize measurement errors, each experiment was conducted in triplicate.

2.5. Density Functional Theory (DFT) Calculations

The DFT simulations were performed in the Materials Studio software using the CASTEP module. For the construction of surface models, the thickness of the vacuum slab was set to 20 Å. ZnO (101) and g-C_3N_5 (002) were constructed as input models. The exchange-correlation interaction was defined by generalized gradient approximation (GGA) parameterized with the Perdew-Burke-Ernzerhof (PBE) functional. The energy cutoff was set to 630 eV, and the Monkhorst-Pack k-point mesh was set to Gamma point. The atom convergence tolerance was set to 2×10^{-6} eV [23].

3. Results and Discussion

3.1. Characterization of Catalysts

The phase structure of the catalysts was determined by XRD analysis. As illustrated in Figure 2a, the peaks of ZnO at 31.7°, 34.5°, 36.2°, 47.3°, 56.5°, 62.7°, and 67.9° correspond to the crystal planes (100), (002), (101), (102), (110), (103), and (112), which are in perfect agreement with the hexagonal wurtzite crystalline phase (JCPDS NO. 36-1451) [24]. In the case of g-C_3N_5, a distinct peak at 27.4° is assigned to the (002) plane, corresponding to the π–π interlayer stacking of carbon nitride [25]. The XRD pattern of the synthesized ZCN sample reveals distinct diffraction peaks characteristic of ZnO (denoted by rhombus symbols) and g-C_3N_5 (denoted by a star symbol). This confirms that the in situ synthesis of ZnO on g-C_3N_5 successfully forms a heterojunction without altering the fundamental structures of

either ZnO or g-C_3N_5. Furthermore, FTIR spectroscopy was used to investigate the surface functional groups of the catalysts. As illustrated in Figure 2b, ZnO exhibits a broad peak in the range of 430–530 cm^{-1}, which is attributed to the Zn-O stretching vibrations [26]. The peaks of ZnO observed in the range of 1430–1580 cm^{-1} are assigned to the stretching vibrations of C=O and the bending vibrations of O-H, respectively [27]. For g-C_3N_5, a sharp characteristic peak at 810 cm^{-1} corresponds to the condensed C-N heterocycles of the triazine moiety [28]. The peaks within the range of 1240–1630 cm^{-1} are associated with C=N and C-N stretching vibrations in the triazole and triazine rings [29], while the characteristic peaks at 3000 and 3600 cm^{-1} are ascribed to residual -NH_2 groups [30]. Notably, the ZCN exhibits the characteristic peaks of both g-C_3N_5 and ZnO, without the appearance of any additional peaks, indicating the successful synthesis of the composite material with high purity.

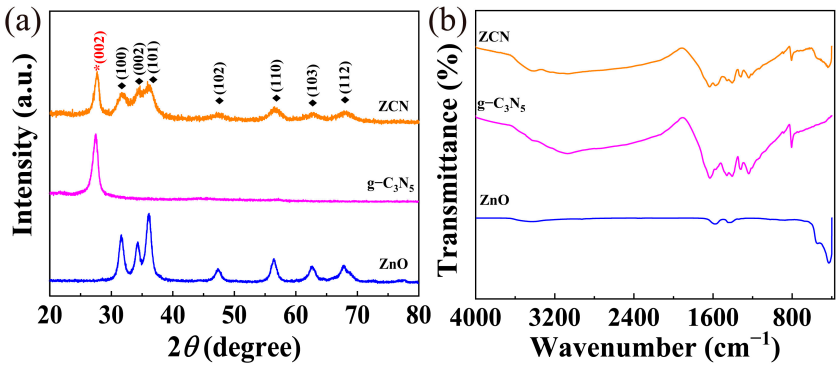

Figure 2. (**a**) XRD and (**b**) FTIR spectra of ZnO, g-C_3N_5, and ZCN samples.

The SEM images of ZnO, g-C_3N_5, and ZCN samples are shown in Figure 3. As illustrated in Figure 3a, ZnO exhibits a spherical morphology with an average diameter of approximately 5–7 µm. In Figure 3b, the g-C_3N_5 nanostructure displays a block-like structure stacked by nanosheets. Figure 3c,d reveals that the introduction of g-C_3N_5 alters the morphology of ZnO to a certain extent, leading to the formation of a porous honeycomb-like structure.

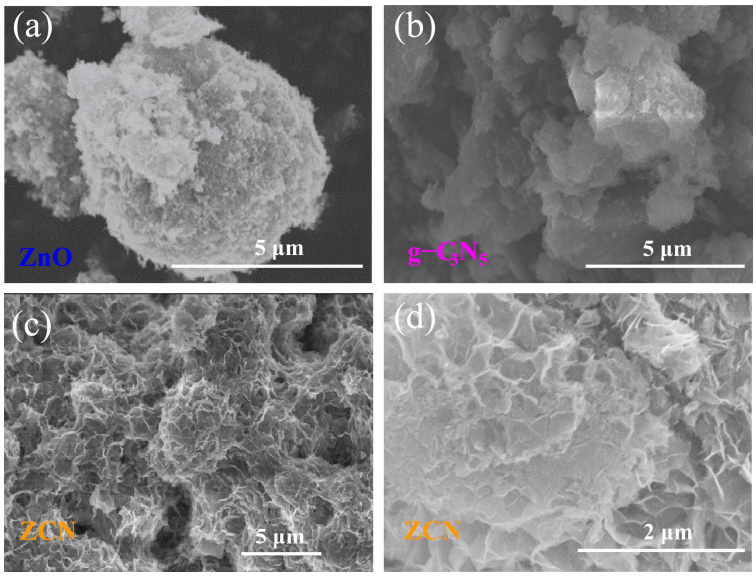

Figure 3. (**a**) SEM images of (**a**) ZnO and (**b**) g-C_3N_5 and (**c**), (**d**) ZCN samples at different magnifications.

The surface area characteristics of ZnO, g-C_3N_5, and ZCN samples were analyzed by using BET analysis based on N_2 adsorption-desorption isotherms. As shown in Figure 4, all

the samples exhibit a typical type IV isotherm with an H3 hysteresis loop [31], indicating the existence of lamellar or sheet-like structures. From the BJH pore size distribution plots (the insets of Figure 4), it can be observed that they are mesoporous materials. As listed in Table S1, ZnO demonstrates a significantly higher adsorption capacity compared to the other two samples, owing to its porous spherical structure. After the construction of a heterojunction between ZnO and g-C_3N_5, a slight reduction in the S_{BET} value is observed, which can be attributed to the fact that a small amount pores of ZnO are occupied by g-C_3N_5.

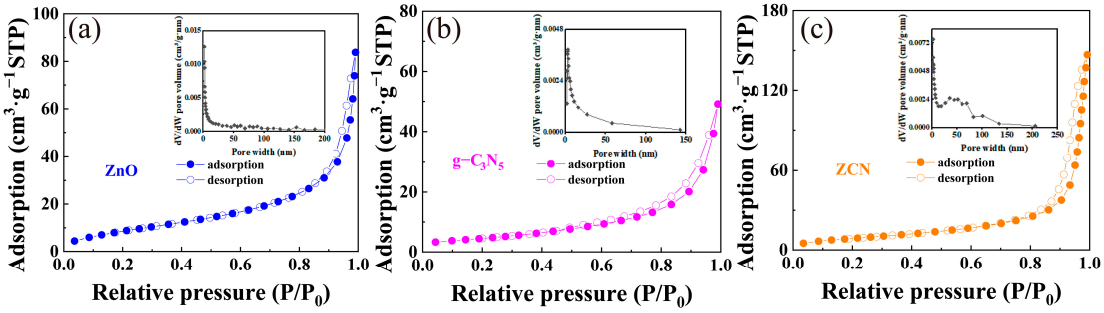

Figure 4. N_2 adsorption–desorption isotherms and pore size distribution of (**a**) ZnO, (**b**) g-C_3N_5, and (**c**) ZCN samples.

3.2. Photocatalytic Performance

As illustrated in Figure 5, the photocatalytic performance of the ZnO, g-C_3N_5, and ZCN samples was investigated by degrading the MB under simulated sunlight irradiation. As shown in Figure 5a, 16% MB can be degraded within 70 min in the absence of photocatalysts. Notably, the MB removal efficiencies are significantly enhanced after the introduction of photocatalysts. After 70 min of photocatalysis, the MB degradation rates in the pure g-C_3N_5 system and ZnO system are 70% and 78%, respectively, while the ZCN system achieves a significantly higher degradation rate exceeding 97%. To further illustrate the changes in organic matter concentration during the degradation process, the time-dependent absorbance variations of the MB solution were monitored at a 10 min interval using the ZCN catalyst as a representative, as displayed in Figure 5b. The corresponding degradation kinetics were also calculated, and the results are shown in Figure 5c,d. The kinetic constant of the ZCN system is 0.0433 min^{-1}, which is 1.9 times and 2.6 times that of the ZnO system and g-C_3N_5 system, respectively. In scientific research, the evaluation of catalytic performance predominantly focuses on the catalyst's stability and its recyclability. As shown in Figure 5e,f, the MB removal efficiency by ZCN remained over 88% after four cycles under simulated sunlight, demonstrating the excellent stability of ZCN. However, for the fifth cycle, the MB degradation efficiency declined to approximately 78%, which could be attributed to catalyst loss, photo-corrosion during recycling, and competitive adsorption on the catalyst surface. Subsequently, we compared our research findings with those of previous studies, as summarized in Table 1. The results indicated that it took more than 100 min to achieve 80% efficiency or higher in approximately two-thirds of the reports, regardless of whether ZnO or g-C_3N_5 was used in composite materials. Our work demonstrated a degradation efficiency exceeding 97% within 70 min with the ZCN photocatalyst.

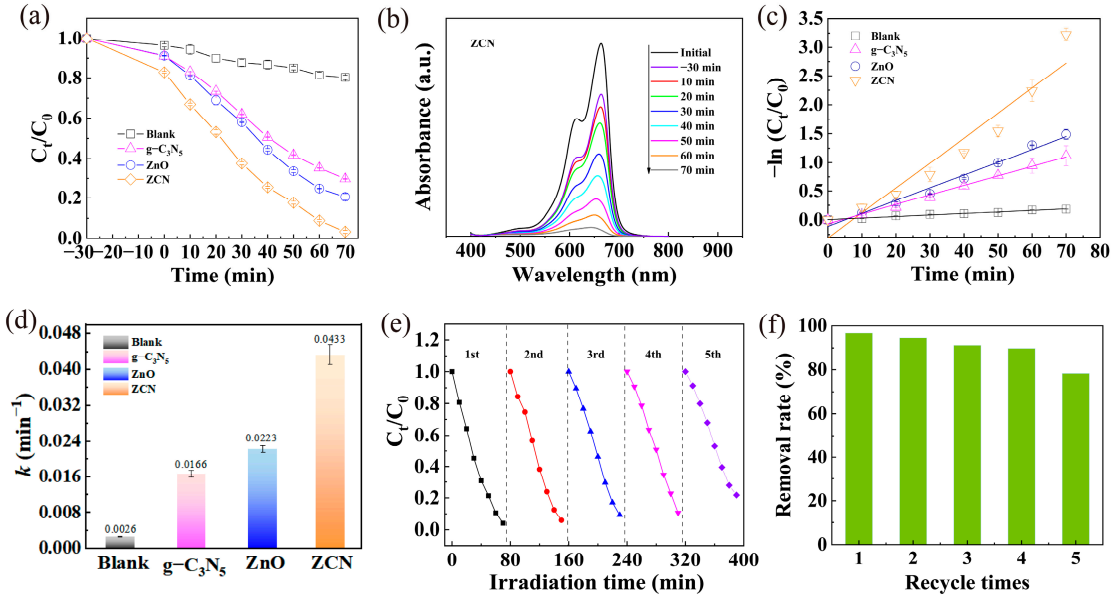

Figure 5. (**a**) Photocatalytic performance of ZnO, g-C_3N_5, and ZCN samples; (**b**) UV-visible absorption spectrum of MB solution degraded by ZCN; (**c**) degradation kinetic plots for the photodegradation of MB; (**d**) degradation kinetic constants of different samples. (**e**,**f**) Five cycles of MB solution degraded by ZCN. Condition: c_{MB} = 30 mg·L^{-1}; c_{cat} = 0.2 g·L^{-1}.

Table 1. Comparison of MB degradation performance of ZCN with some reported ZnO and g-C_3N_5 catalytic systems.

System	Condition	Time	Degradation Percentage	Ref.
ZCN	300 W Xe lamp, $[MB]_0$ = 30 mg·L^{-1}, $[Catalyst]_0$ = 0.2 g·L^{-1}	70 min	97%	This work
TiO_2/ZnO/rGO	300 W Xe lamp, $[MB]_0$ = 20 mg·L^{-1}, $[Catalyst]_0$ = 0.5 g·L^{-1}	180 min	~80%	[8]
Cu-ZnO	300 W Xe lamp, $[MB]_0$ = 5 mg·L^{-1}, $[Catalyst]_0$ = 0.5 g·L^{-1}	90 min	~81%	[32]
ZnO: Eu (10%)-M	300 W Xe lamp, $[MB]_0$ = 10 mg·L^{-1}, $[Catalyst]_0$ = 1 g·L^{-1}	150 min	~90%	[15]
3wt % Cu-doped ZnO ($CuZn_3$)	300 W Xe lamp, $[MB]_0$ = 10 mg·L^{-1}, $[Catalyst]_0$ = 0.1 g·L^{-1}	180 min	92%	[33]
ZnO/SnO_2/carbon	300 W Xe lamp, $[MB]_0$ = 25 mg·L^{-1}, $[Catalyst]_0$ = 3.6 g·L^{-1}	300 min	~50%	[34]
ZnO-Cu-CuO/C_3N_4	300 W Xe lamp, $[MB]_0$ = 30 mg·L^{-1}, $[Catalyst]_0$ = 0.2 g·L^{-1}	120 min	~75%	[35]
ZnO/g-C_3N_4	300 W Xe lamp, $[MB]_0$ = 5 mg·L^{-1}, $[Catalyst]_0$ = 0.4 g·L^{-1}	100 min	~80%	[36]
TiO_2/g-C_3N_5	500 W Xe lamp, $[MB]_0$ = 20 mg·L^{-1}, $[Catalyst]_0$ = 2.5 g·L^{-1}	180 min	97%	[37]
g-C_3N_5/MK30	300 W Xe lamp, $[MB]_0$ = 10 mg·L^{-1}, $[Catalyst]_0$ = 0.2 g·L^{-1}	40 min	90%	[38]

These results demonstrate the superior photocatalytic performance of the ZCN heterojunction compared to ZnO and g-C_3N_5, which can be employed as a promising material applied for the photocatalytic degradation of organic compounds.

3.3. Photocatalytic Mechanism Exploration

The photocatalytic performance of photocatalysts is primarily influenced by their light absorption capacity and the efficiency of photogenerated electron–hole pair separation under illumination [39]. Therefore, the enhanced degradation mechanism of the honeycomb-like ZCN heterojunction was investigated via these two fundamental perspectives.

To determine the light absorption capacity of the materials, the UV-vis DRS spectra of ZnO, g-C_3N_5, and ZCN were recorded (Figure 6a). ZnO only absorbs UV light with an absorption edge located at 395 nm, which aligns well with previously reported findings for ZnO [40]. The absorption edges of g-C_3N_5 and ZCN are approximately 720 and 710 nm, respectively. In comparison to ZnO, the absorption spectrum of ZCN exhibits a significant redshift, signifying an enhanced visible light absorption range for ZnO upon the formation of a heterojunction with g-C_3N_5. The bandgap values of the synthesized samples were further determined using the Tauc model, described by the following equation [41]:

$$\alpha h\nu = A(h\nu - E_g)^{n/2} \quad (1)$$

where α is the absorption coefficient, $h\nu$ is the photon energy, E_g represents the bandgap energy, A is a proportionality constant, and n depends on the type of electronic transition (n = 1 for direct leaps, while n = 4 for indirect leaps). According to previous studies, ZnO is a direct bandgap semiconductor, characterized by an n value of 1, while g-C_3N_5 acts as an indirect bandgap semiconductor with an n value of 4 [42,43]. As illustrated in Figure 6b,c, the bandgap energy (E_g) values for ZnO, g-C_3N_5, and ZCN were determined from the Tauc plots by extrapolating the linear tangent to the abscissa. The estimated E_g values are 3.20, 2.16, and 2.79 eV for ZnO, g-C_3N_5, and ZCN, respectively. Based on the valence band XPS (VB-XPS) spectra (Figure 6d,e), the conduction band (CB) positions of the catalysts were calculated and are presented in Figure 6f. The narrower energy gap of g-C_3N_5 suggests its enhanced capability for efficient potential-driven electron transfer to ZnO.

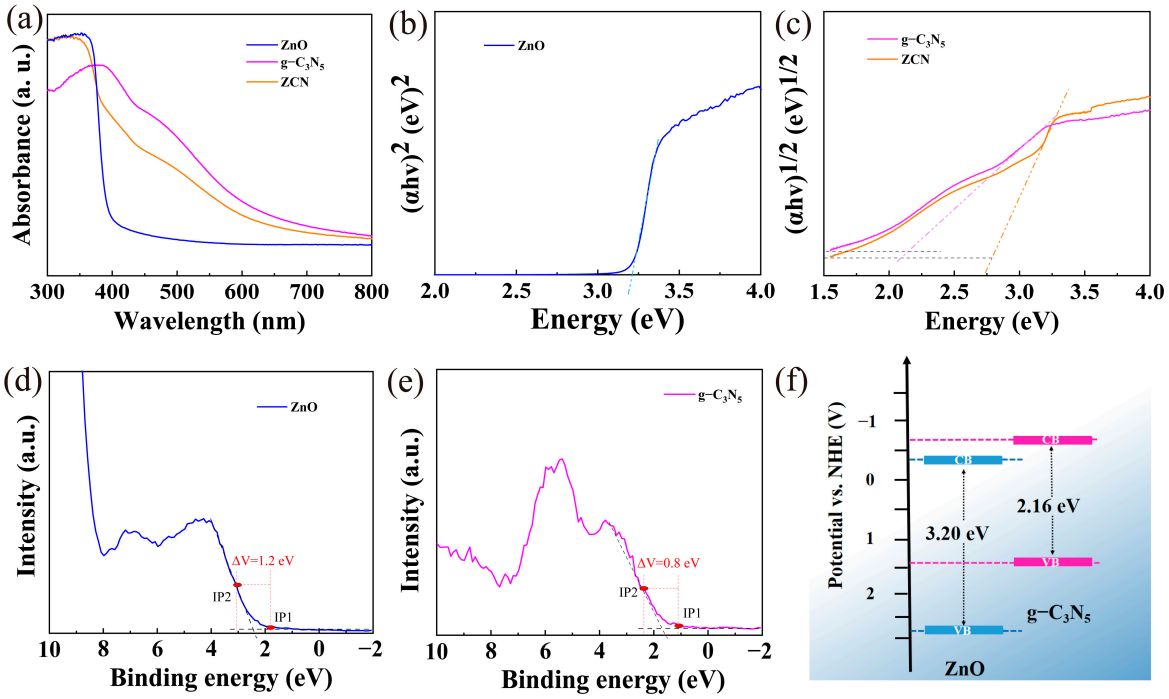

Figure 6. (**a**) UV-vis DRS; (**b**,**c**) corresponding Tauc's plots; (**d**,**e**) VB-XPS spectra; (**f**) illustration of the band structure of ZnO, g-C_3N_5, and ZCN samples.

When semiconductors are exposed to light, electrons in the VB are excited to the CB, resulting in the generation of electron-hole pairs. However, if these charge carriers are not effectively utilized, they tend to recombine rapidly, leading to their annihilation. Thus, effective separation of photogenerated electrons and holes is essential for semiconductors to achieve enhanced photocatalytic performance under light irradiation. PL is a well-established method for characterizing the recombination efficiency of photogenerated electron-hole pairs, and thus the room-temperature measurements were performed using an excitation wavelength of 320 nm, as depicted in Figure 7. ZCN presents two emission peaks at 380 and 435 nm, corresponding to the characteristics of ZnO and g-C_3N_5, respectively [44]. Compared to ZnO and g-C_3N_5, ZCN exhibits the significantly lower PL intensity, indicating the lowest recombination rate of photogenerated electrons. This suggests that the honeycomb-like heterojunction formed through the in situ synthesis of ZnO on g-C_3N_5 significantly enhances the photogenerated electron separation efficiency of ZnO.

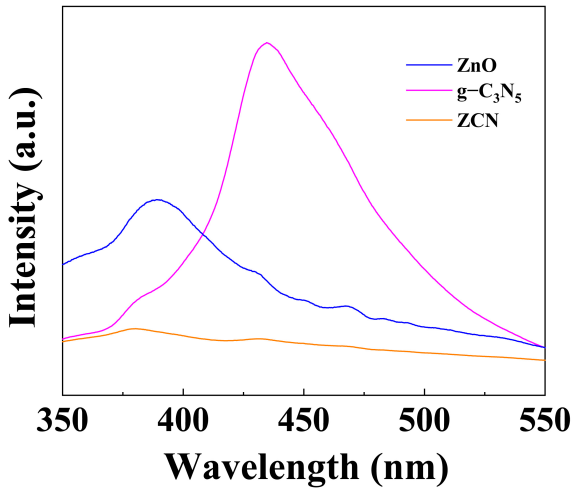

Figure 7. PL spectra of ZnO, g-C_3N_5, and ZCN samples.

To gain deeper insight into the electron transfer process between ZnO and g-C_3N_5, XPS was employed to compare the spectra of ZCN with those of pure ZnO and g-C_3N_5. Figure 8a shows the high-resolution Zn 2p spectrum of ZnO, and it displays the characteristic peaks at 1021.98 and 1045.07 eV, ascribed to the Zn $2p_{1/2}$ and Zn $2p_{3/2}$ orbits, respectively [45]. The corresponding peaks shift to 1021.88 and 1044.94 eV for ZCN, suggesting electron transfer from g-C_3N_5 to ZnO in the composite, resulting in the formation of a built-in electric field from g-C_3N_5 to ZnO. The O 1s spectrum of ZnO displayed in Figure 8b can be deconvoluted into three peaks at 530.28, 531.75, and 534.04 eV, attributed to lattice oxygen bound to Zn, oxygen vacancies, and adsorbed H_2O, respectively [46,47]. The change in binding state of O is generally not employed to determine the built-in electric field due to the low intensity of the peak compared to Zn according to previous research [27]. Nevertheless, the peak of oxygen vacancies (531.75–532.10 eV) is significantly enlarged for ZCN. It indicates an enhanced probability of electron capture by defective energy levels in the ZCN. These findings further confirm that the honeycomb-like ZCN heterojunction exhibits excellent separation efficiency for photogenerated electron–hole pairs. The C 1s spectra are displayed in Figure 8c, and the characteristic peak of g-C_3N_5 at 284.86 eV is attributed to graphitic carbon (C-C), while the peaks at 286.60, 288.18, and 293.45 eV belong to C-NH_2 groups, sp^2-hybridized carbon (N=C-N), and π–π^* bonds, respectively [48,49]. The N 1s spectrum of g-C_3N_5 in Figure 8d can be divided into four peaks at 398.55, 399.54, 400.68, and 404.57 eV ascribed to the terminal C-N=C, tertiary N-$(C)_3$, amino groups, and

π–π* bond, respectively [49]. The binding energies of C 1s and N 1s in the ZCN both shift toward higher energies to different degrees, indicating electron loss from C and N in the ZCN. Again, this result confirms that electrons transfer from g-C_3N_5 to ZnO.

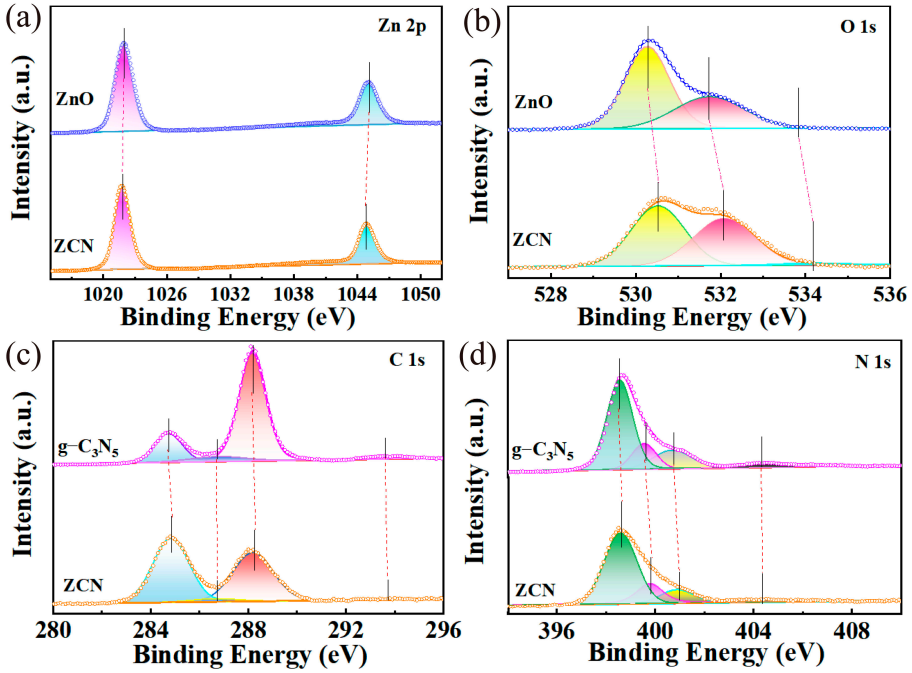

Figure 8. (**a**) Zn 2p, (**b**) O 1s, (**c**) C 1s, and (**d**) N 1s XPS spectra of ZCN compared with ZnO and g-C_3N_5.

The work function (Φ) of a catalyst is a key parameter related to its charge transfer ability, which is related to the contact potential difference (ΔV) expressed by the following equation [50]:

$$\Delta V = \Phi - \varphi \quad (2)$$

where φ is the work function of the instrument. ΔV is associated with the binding energy of electrons, which influences the kinetic energy of free electrons. It can be calculated through the distance of inflection points (IPs) in the VB-XPS spectrum [51]. As shown in Figure 6d,e, the ΔV for ZnO and g-C_3N_5 is 1.2 and 0.8 eV, respectively. This indicates that g-C_3N_5 has a higher Fermi energy level (EF) and smaller work function than ZnO, suggesting that electrons can transfer readily from g-C_3N_5 to ZnO.

Moreover, the EF of ZnO and g-C_3N_5 was estimated by DFT calculations, as illustrated in Figure 9a,b. The larger EF of ZnO signifies that the electrons are more likely to escape from g-C_3N_5 to ZnO at the interface. Consequently, as shown in Figure 9c,d, upon contact between ZnO and g-C_3N_5, electrons from g-C_3N_5 are transferred to ZnO until their Fermi levels reach equilibrium. This process results in the formation of an internal electric field (IEF) at their interface and, thereby, the band bending of ZnO and g-C_3N_5. This promotes the recombination of electrons in the CB of ZnO (CB_{ZnO}) with holes in the VB of g-C_3N_5 (VB_{CN}) under simulated sunlight irradiation, effectively suppressing the recombination of photogenerated charge carriers within their respective semiconductors. Finally, the photogenerated carriers at the interface establish a Z-scheme pathway, with accumulated electrons and holes localized at the CB of g-C_3N_5 (CB_{CN}) and the VB of ZnO (VB_{ZnO}), respectively.

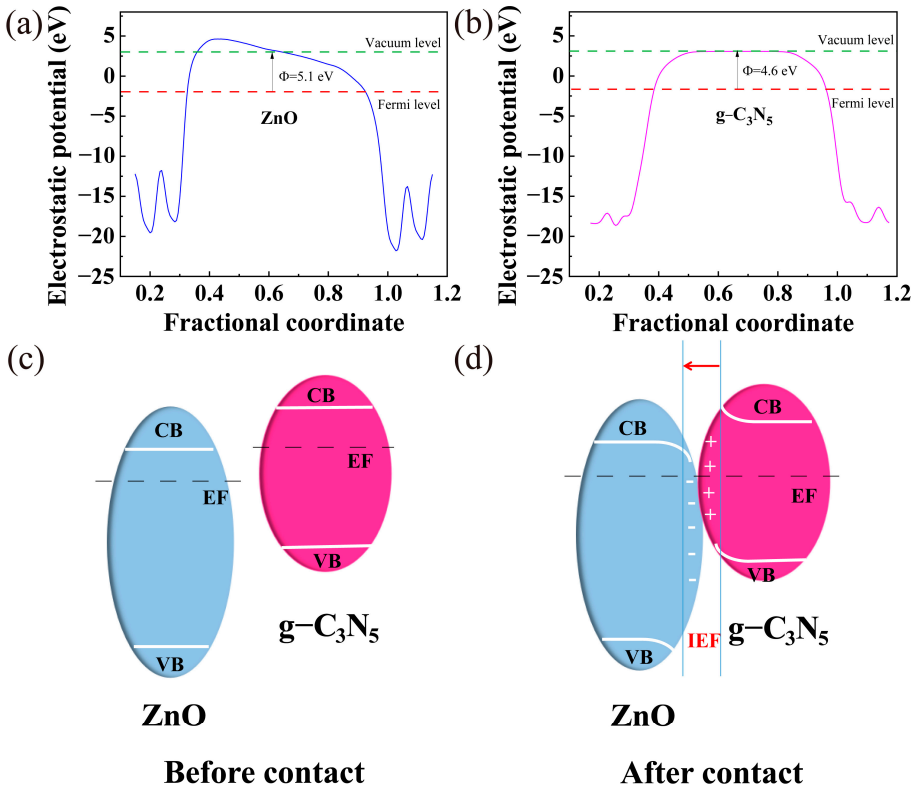

Figure 9. DFT-calculated electrostatic potentials of (**a**) ZnO and (**b**) g-C_3N_5 by DFT. (**c**,**d**) Energy band configuration between ZnO and g-C_3N_5.

To further elucidate the Z-scheme pathway mechanism, ESR spectroscopy was employed by using DMPO as the capture agent for O_2^- and OH. The DMPO-O_2^- patterns displayed in Figure 10a clearly exhibit a distinct signal corresponding to O_2^- ($E^0_{O_2/O_2^-} = -0.16$ V) [52], generated by the g-C_3N_5 ($E_{CB\text{-}CN} = -0.67$ V) of the ZCN heterojunction during the photocatalytic process. As shown in Figure 10b, a DMPO-OH signal can be seen, indicating that water is oxidized to OH under light irradiation. Given that the VB position of g-C_3N_5 ($E_{VB\text{-}CN} = 1.49$ V) is lower than the oxidation potential of water ($E^0_{H_2O/OH} = 2.3$ V) and the VB position of ZnO ($E_{VB\text{-}ZnO} = 2.78$ V) is higher, the ZnO-generated holes can oxidize water, but the g-C_3N_5-generated holes cannot. Thus, only the VB of ZnO contributes to the generation of OH during the photocatalytic degradation of MB using the ZCN heterojunction. Obviously, these results not only confirm the Z-scheme pathway mechanism but also prove that O_2^- and OH were involved in the degradation process.

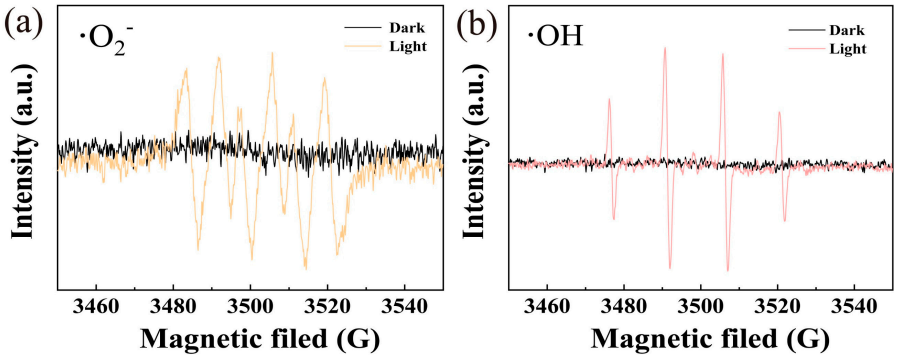

Figure 10. ESR signals of (**a**) DMPO-OH; (**b**) DMPO-O_2^- in the solution with ZCN under different conditions.

Based on the aforementioned results and findings, a photocatalytic mechanism is suggested and depicted in Figure 11. Upon simulated sunlight irradiation (hv), electrons in the ZCN heterojunction are excited from the VB to the CB. The IEF at the interface facilitates the recombination of electrons from the CB of ZnO (e^-_{ZnO}) with holes in the VB of g-C_3N_5 (h^+_{CN}). The remaining holes in the VB of ZnO (h^+_{ZnO}) and the electrons in the CB of g-C_3N_5 (e^-_{CN}) then participate in redox reactions, resulting in the degradation of MB pollutants into water and carbon dioxide. This photodegradation process is summarized by Equations (3)–(8) [20].

$$\text{g-}C_3N_5 + hv \rightarrow e^-_{CN} + h^+_{CN} \quad (3)$$

$$ZnO + hv \rightarrow e^-_{ZnO} + h^+_{ZnO} \quad (4)$$

$$e^-_{ZnO} + h^+_{CN} \rightarrow \text{Z} - \text{scheme pathway recombination} \quad (5)$$

$$e^-_{CN} + O_2 \rightarrow O_2^- \quad (6)$$

$$h^+_{ZnO} + H_2O \rightarrow OH + H^+ \quad (7)$$

$$O_2^-/OH/h^+_{ZnO} + \text{MB} \rightarrow \text{intermediates} + CO_2 + H_2O \quad (8)$$

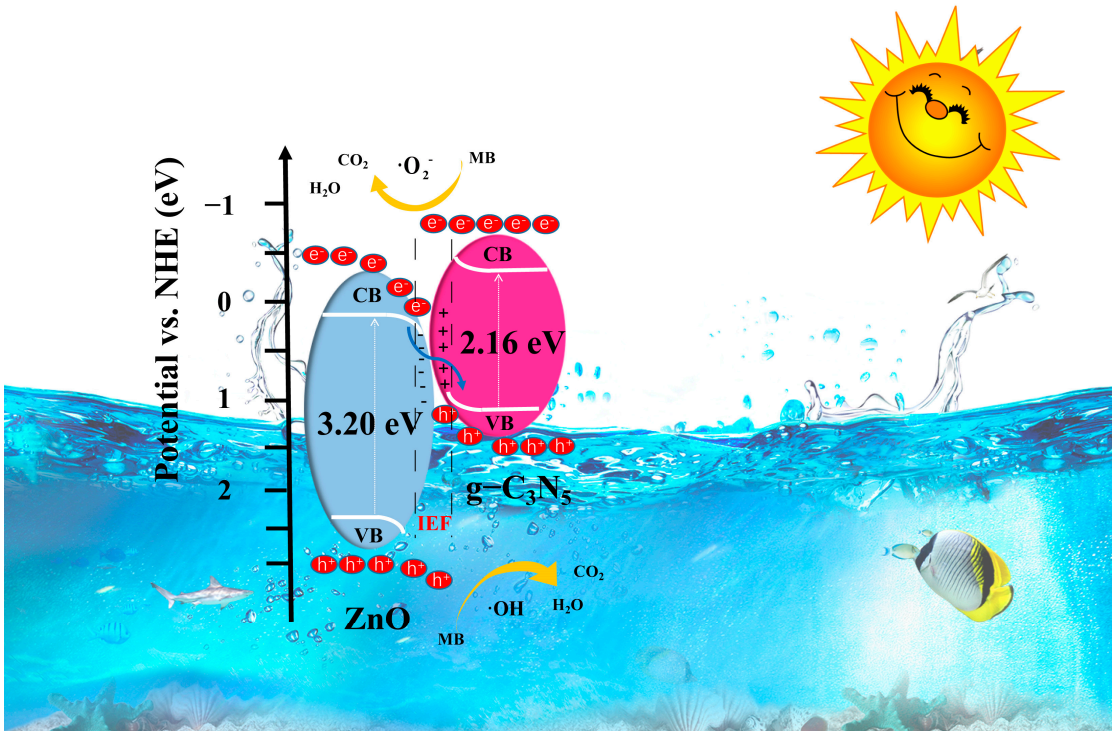

Figure 11. The mechanism of MB degradation with a ZCN heterojunction under simulated sunlight irradiation.

4. Conclusions

In this study, a honeycomb-like ZCN heterojunction with a Z-scheme energy band configuration was synthesized over g-C_3N_5 in situ using a combination of calcination and hydrothermal methods. The ZCN photocatalyst exhibited significantly enhanced kinetics (k = 0.0433 min^{-1}) for MB degradation, which were 1.9 times that of pure ZnO (k = 0.0223 min^{-1}). The remarkable photocatalytic performance of ZCN can be attributed to two key factors. First, the ZCN heterojunction facilitates efficient photon absorption up to 710 nm, which broadens the adsorption edge of ZnO to the visible light region. Second, the Z-scheme heterojunction effectively suppresses charge carrier recombination,

while it preserves the strong redox capacity of both g-C_3N_5 and ZnO, as confirmed by ESR experimental data and DFT simulations. This study presents a potential approach for the design and development of highly efficient Z-scheme photocatalysts for environmental remediation. Nevertheless, this study was conducted under laboratory conditions without testing on actual wastewater, which highlights the need for future research to address this gap.

Supplementary Materials: The following supporting information can be downloaded at https://www.mdpi.com/article/10.3390/pr13010253/s1: Table S1: Textural properties of the samples. Figure S1: Photocatalytic performance of ZnO, g-C3N5, and ZCN samples. Condition: cMB = 10 mg·L^{-1}; ccat = 0.2 g·L^{-1}.

Author Contributions: Conceptualization, S.L. (Sitong Liu); methodology, S.L. (Sitong Liu); software, X.W.; validation, S.L. (Sitong Liu); formal analysis, S.L. (Sitong Liu), S.L. (Shicheng Liu), X.W., L.L., L.Y., R.R., H.W. and Z.S.; investigation, S.L. (Sitong Liu); resources, X.W.; data curation, S.L. (Sitong Liu); writing—original draft preparation, S.L. (Sitong Liu), S.L. (Shicheng Liu); writing—review and editing, S.L. (Sitong Liu), S.L. (Shicheng Liu) and X.W.; visualization, S.L. (Sitong Liu); supervision, X.W.; project administration, X.W.; funding acquisition, X.W. All authors have read and agreed to the published version of the manuscript.

Funding: This research was funded by the National Natural Science Foundation of China (Grant No. 22279072).

Data Availability Statement: Dataset available on request from the authors.

Acknowledgments: The authors extend their gratitude to Qiling Cai from Shiyanjia Lab (www.Shiyanjia.com (accessed on 1 December 2024)) for providing invaluable assistance with XPS analysis.

Conflicts of Interest: The authors declare no conflicts of interest.

References

1. Dihom, H.R.; Al-Shaibani, M.M.; Radin Mohamed, R.M.S.; Al-Gheethi, A.A.; Sharma, A.; Khamidun, M.H.B. Photocatalytic degradation of disperse azo dyes in textile wastewater using green zinc oxide nanoparticles synthesized in plant extract: A critical review. *J. Water Process Eng.* **2022**, *47*, 102705. [CrossRef]
2. Medina-Acosta, M.; Chinchillas-Chinchillas, M.J.; Garrafa-Gálvez, H.E.; Garcia-Maro, C.A.; Rosas-Casarez, C.A.; Lugo-Medina, E.; Luque-Morales, P.A.; Soto-Robles, C.A. Photocatalytic Degradation of Four Organic Dyes Present in Water Using ZnO Nanoparticles Synthesized with Green Synthesis Using Ambrosia ambrosioides Leaf and Root Extract. *Processes* **2024**, *12*, 2456. [CrossRef]
3. Chakraborty, S.; De, S.; Basu, J.K.; DasGupta, S. Treatment of a textile effluent: Application of a combination method involving adsorption and nanofiltration. *Desalination* **2005**, *174*, 73–85. [CrossRef]
4. Mohammed, H.A.; Khaleefa Ali, S.A.; Basheer, M.I. Heavy metal ions removal using advanced oxidation (UV/H_2O_2) technique. *IOP Conf. Ser. Mater. Sci. Eng.* **2020**, *870*, 012026. [CrossRef]
5. Ihaddaden, S.; Aberkane, D.; Boukerroui, A.; Robert, D. Removal of methylene blue (basic dye) by coagulation-flocculation with biomaterials (bentonite and Opuntia ficus indica). *J. Water Process Eng.* **2022**, *49*, 102952. [CrossRef]
6. Rafatullah, M.; Sulaiman, O.; Hashim, R.; Ahmad, A. Adsorption of methylene blue on low-cost adsorbents: A review. *J. Hazard. Mater.* **2010**, *177*, 70–80. [CrossRef]
7. Rashid, M.; Al-Zaqri, N.; Guerrero-Barajas, C.; Hussain, F.; Ibrahim, M.N. Waste Derived Graphene Oxide-ZnO: An Efficient Photocatalyst for Rhodamine 6G. *Processes* **2022**, *10*, 2266. [CrossRef]
8. Nguyen, C.H.; Tran, M.L.; Tran, T.T.V.; Juang, R.-S. Enhanced removal of various dyes from aqueous solutions by UV and simulated solar photocatalysis over TiO_2/ZnO/rGO composites. *Sep. Purif. Technol.* **2020**, *232*, 115962. [CrossRef]
9. Tichapondwa, S.M.; Newman, J.P.; Kubheka, O. Effect of TiO_2 phase on the photocatalytic degradation of methylene blue dye. *Phys. Chem. Earth Parts A/B/C* **2020**, *118–119*, 102900. [CrossRef]
10. Cheng, T.; Gao, H.; Liu, G.; Pu, Z.; Wang, S.; Yi, Z.; Wu, X.; Yang, H. Preparation of core-shell heterojunction photocatalysts by coating CdS nanoparticles onto $Bi_4Ti_3O_{12}$ hierarchical microspheres and their photocatalytic removal of organic pollutants and Cr(VI) ions. *Colloids Surf. A Physicochem. Eng. Asp.* **2022**, *633*, 127918. [CrossRef]

11. Kheirabadi, M.; Samadi, M.; Asadian, E.; Zhou, Y.; Dong, C.; Zhang, J.; Moshfegh, A.Z. Well-designed Ag/ZnO/3D graphene structure for dye removal: Adsorption, photocatalysis and physical separation capabilities. *J. Colloid Interface Sci.* **2019**, *537*, 66–78. [CrossRef] [PubMed]
12. Nawaz, A.; Farhan, A.; Maqbool, F.; Ahmad, H.; Qayyum, W.; Ghazy, E.; Rahdar, A.; Díez-Pascual, A.M.; Fathi-karkan, S. Zinc oxide nanoparticles: Pathways to micropollutant adsorption, dye removal, and antibacterial actions—A study of mechanisms, challenges, and future prospects. *J. Mol. Struct.* **2024**, *1312*, 138545. [CrossRef]
13. Yashni, G.; Al-Gheethi, A.; Radin Mohamed, R.M.S.; Dai-Viet, N.V.; Al-Kahtani, A.A.; Al-Sahari, M.; Nor Hazhar, N.J.; Noman, E.; Alkhadher, S. Bio-inspired ZnO NPs synthesized from Citrus sinensis peels extract for Congo red removal from textile wastewater via photocatalysis: Optimization, mechanisms, techno-economic analysis. *Chemosphere* **2021**, *281*, 130661. [CrossRef]
14. Sahu, S.K.; Palai, A.; Sahu, D. Photocatalytic applications of metal oxide-based nanocomposites for sustainable environmental remediation. *Sustain. Chem. Environ.* **2024**, *8*, 100162. [CrossRef]
15. Trandafilović, L.V.; Jovanović, D.J.; Zhang, X.; Ptasińska, S.; Dramićanin, M.D. Enhanced photocatalytic degradation of methylene blue and methyl orange by ZnO:Eu nanoparticles. *Appl. Catal. B Environ.* **2017**, *203*, 740–752. [CrossRef]
16. Liu, F.; Zhang, Q.; Chen, C.; Zhang, Z.; Fang, X. Theoretical design and experimental study a novel direct Z-scheme V_2O_5/C_3N_5 heterojunction for efficient photocatalytic hydrogen production. *Sol. Energy Mater. Sol. Cells* **2023**, *257*, 112385. [CrossRef]
17. Liu, D.; Yao, J.; Chen, S.; Zhang, J.; Li, R.; Peng, T. Construction of rGO-coupled C_3N_4/C_3N_5 2D/2D Z-scheme heterojunction to accelerate charge separation for efficient visible light H2 evolution. *Appl. Catal. B Environ.* **2022**, *318*, 121822. [CrossRef]
18. Hu, Y.; Chen, Z.; Jiao, Y.; Chen, W.; Liu, L.; Wang, X. Experimental Investigation of Vitrification Process for the Disposal of Hazardous Solid Waste Containing Chlorides. *Processes* **2022**, *10*, 526. [CrossRef]
19. Chen, S.; Wang, H.; Mo, Z.; Li, S.; Yang, J.; Li, M.; Zhang, H.; Wei, L.; Yang, X. Highly efficient g-C_3N_5/Bi_2MoO_6 heterojunction for aflatoxin B1 photocatalytic degradation. *Inorg. Chem. Commun.* **2024**, *170*, 113156. [CrossRef]
20. Fan, W.; Chang, H.; Zheng, X.; Lu, J.; Yin, G.; Jiang, Z. Elaborate construction of a MOF-derived novel morphology Z-scheme ZnO/ZnCdS heterojunction for enhancing photocatalytic H_2 evolution and tetracycline degradation. *Sep. Purif. Technol.* **2025**, *357*, 130068. [CrossRef]
21. Wang, L.; Chen, R.; Zhang, Z.; Chen, X.; Ding, J.; Zhang, J.; Wan, H.; Guan, G. Constructing direct Z-scheme heterojunction g-C3N5/BiOBr for efficient photocatalytic CO_2 reduction with H_2O. *J. Environ. Chem. Eng.* **2023**, *11*, 109345. [CrossRef]
22. Liu, S.; Wang, W.; Cheng, Y.; Yao, L.; Han, H.; Zhu, T.; Liang, Y.; Fu, J. Methyl orange adsorption from aqueous solutions on 3D hierarchical PbS/ZnO microspheres. *J. Colloid Interface Sci.* **2020**, *574*, 410–420. [CrossRef]
23. Dong, Y.; Mushtaq, N.; Almutairi, B.S.; Shah, M.A.K.Y.; Lu, Y.; Deng, C. Highly improved ionic conduction in reverse spinel structured $CoAl_2O_4$ and ZnO heterostructure through interfacial disordering. *Ceram. Int.* **2024**, *50*, 28113–28122. [CrossRef]
24. El Golli, A.; Fendrich, M.; Bazzanella, N.; Dridi, C.; Miotello, A.; Orlandi, M. Wastewater remediation with ZnO photocatalysts: Green synthesis and solar concentration as an economically and environmentally viable route to application. *J. Environ. Manag.* **2021**, *286*, 112226. [CrossRef]
25. Liu, S.; Liu, S.; Wang, W.; Zhang, C.; Wang, L.; Liang, Y.; Fu, J.; Zhou, Q. Mn-periodate complex in situ formed at Mn-N coordinate site in Mn-doped g-C3N5 for efficient and rapid water purification. *Chem. Eng. J.* **2024**, *498*, 155546. [CrossRef]
26. Liang, M.-K.; Limo, M.J.; Sola-Rabada, A.; Roe, M.J.; Perry, C.C. New Insights into the Mechanism of ZnO Formation from Aqueous Solutions of Zinc Acetate and Zinc Nitrate. *Chem. Mater.* **2014**, *26*, 4119–4129. [CrossRef]
27. Yu, F.; Zhang, J.; Ren, J.; Chen, H.; Tian, X.; Feng, C.; Li, C.; Zhang, J.; Tang, X.; Hou, X. ZnO@g-C_3N_4 photocatalyst with switchable carrier transfer mechanism between type-II and S-scheme through S doping. *J. Alloys Compd.* **2024**, *982*, 173756. [CrossRef]
28. Kim, I.Y.; Kim, S.; Jin, X.; Premkumar, S.; Chandra, G.; Lee, N.-S.; Mane, G.P.; Hwang, S.-J.; Umapathy, S.; Vinu, A. Ordered Mesoporous C_3N_5 with a Combined Triazole and Triazine Framework and Its Graphene Hybrids for the Oxygen Reduction Reaction (ORR). *Angew. Chem. Int. Ed.* **2018**, *57*, 17135–17140. [CrossRef]
29. Zhang, Z.; Ji, R.; Sun, Q.; He, J.; Chen, D.; Li, N.; Li, H.; Marcomini, A.; Xu, Q.; Lu, J. Enhanced photocatalytic degradation of 2-chlorophenol over Z-scheme heterojunction of CdS-decorated oxygen-doped g-C3N4 under visible-light. *Appl. Catal. B Environ.* **2023**, *324*, 122276. [CrossRef]
30. Li, F.; Huang, T.; Sun, F.; Chen, L.; Li, P.; Shao, F.; Yang, X.; Liu, W. Ferric oxide nanoclusters with low-spin FeIII anchored g-C_3N_4 rod for boosting photocatalytic activity and degradation of diclofenac in water under solar light. *Appl. Catal. B Environ.* **2022**, *317*, 121725. [CrossRef]
31. Liang, H.; Wang, H.; Wang, A.; Cheng, R.; Jing, S.; Chen, F.; Kannan, P.; Balkourani, G.; Tsiakaras, P. Efficient photocatalytic hydrogen peroxide production over S-scheme In_2S_3/molten salt modified C_3N_5 heterojunction. *J. Colloid Interface Sci.* **2024**, *669*, 506–517. [CrossRef] [PubMed]
32. Qi, K.; Xing, X.; Zada, A.; Li, M.; Wang, Q.; Liu, S.; Lin, H.; Wang, G. Transition metal doped ZnO nanoparticles with enhanced photocatalytic and antibacterial performances: Experimental and DFT studies. *Ceram. Int.* **2020**, *46*, 1494–1502. [CrossRef]
33. Sajjadi, S.M.; Hossinzadeh, G. Textile dyes removing from the wastewater by green synthesized Cu-doped ZnO photocatalysts under the simulated sunlight illumination. *Ceram. Int.* **2024**, *50*, 36271–36285. [CrossRef]

34. de Moraes, N.P.; Pereira, R.A.; da Silva, T.V.C.; da Silva, B.H.B.; de Assis, G.P.; Campos, T.M.B.; Thim, G.P.; de Vasconcelos Lanza, M.R.; de Freitas, L.; Rodrigues, L.A. Cross-linked cellulose beads as an eco-friendly support for ZnO/SnO_2/carbon xerogel hybrid photocatalyst: Exploring the synergy between adsorption and photocatalysis under simulated sunlight. *Int. J. Biol. Macromol.* **2024**, *254*, 127826. [CrossRef]
35. Abbasi, E.; Haghighi, M.; Shabani, M.; Niyati, A.; Mahboob, S. Boosted ultrasound-sunlight-driven removal of organic pollutant over double Z-scheme plasmonic ZnO–Cu–CuO/g-C_3N_4 nanophotocatalyst: Design via in-situ co-precipitation hybrid with various sonication powers. *Mater. Today Sustain.* **2023**, *24*, 100580. [CrossRef]
36. Girish, Y.R.; Udayabhanu; Byrappa, N.M.; Alnaggar, G.; Hezam, A.; Nagaraju, G.; Pramoda, K.; Byrappa, K. Rapid and facile synthesis of Z-scheme ZnO/g-C_3N_4 heterostructure as efficient visible light-driven photocatalysts for dye degradation and hydrogen evolution reaction. *J. Hazard. Mater. Adv.* **2023**, *9*, 100230. [CrossRef]
37. Liu, S.; Bu, Y.; Cheng, S.; Tao, R. Synthesis of TiO_2/g-C_3N_5 heterojunction for photocatalytic degradation of methylene blue wastewater under visible light irradiation: Mechanism analysis. *Diam. Relat. Mater.* **2023**, *136*, 110062. [CrossRef]
38. Chellapandi, T.; Madhumitha, G.; Roopan, S.M.; Manjupriya, R.; Arunachalapandi, M.; Pouthika, K.; Elamathi, M. Facile synthesis route for visible active g-C_3N_5/MK30 nanocomposite and its computationally guided photocatalytic degradation of organic pollutants. *Sep. Purif. Technol.* **2023**, *307*, 122865. [CrossRef]
39. Tuama, A.N.; Alzubaidi, L.H.; Jameel, M.H.; Abass, K.H.; bin Mayzan, M.Z.H.; Salman, Z.N. Impact of electron–hole recombination mechanism on the photocatalytic performance of ZnO in water treatment: A review. *J. Sol-Gel Sci. Technol.* **2024**, *110*, 792–806. [CrossRef]
40. Jiang, T.; Lin, M.; He, S.; Xu, T.; Fu, J.; Sun, J.; Zhang, S.; Liang, Y.; Wang, L.; Wang, W. Non-metallic plasmonic effect and step-like charge transport channel synergistically accelerate surface reaction kinetics and charge separation of TiN/CdS-sensitized ZnO photoanode for efficient photoelectrochemical hydrogen evolution. *Appl. Catal. B Environ. Energy* **2025**, *361*, 124631. [CrossRef]
41. Bahiraei, H.; Azarakhsh, S.; Ghasemi, S. Ternary $CoFe_2O_4$/g-C_3N_4/ZnO heterostructure as an efficient and magnetically separable visible-light photocatalyst: Characterization, dye purification, and mechanism. *Ceram. Int.* **2023**, *49*, 21050–21059. [CrossRef]
42. Wang, X.; Yang, S.; Jin, P.; Peng, A.; Zhao, X.; Yang, K.; He, J. Highly efficient photocatalytic degradation of microcystin-LR with permonosulfate activated by visible-light over Z-scheme ZnO/g-C_3N_4: Degradation pathways and mechanism. *J. Environ. Chem. Eng.* **2023**, *11*, 111088. [CrossRef]
43. Li, K.; Cai, W.; Zhang, Z.; Xie, H.; Zhong, Q.; Qu, H. Boron doped C_3N_5 for photocatalytic nitrogen fixation to ammonia: The key role of boron in nitrogen activation and mechanism. *Chem. Eng. J.* **2022**, *435*, 135017. [CrossRef]
44. Li, M.; Lu, Q.; Liu, M.; Yin, P.; Wu, C.; Li, H.; Zhang, Y.; Yao, S. Photoinduced Charge Separation via the Double-Electron Transfer Mechanism in Nitrogen Vacancies g-C_3N_5/BiOBr for the Photoelectrochemical Nitrogen Reduction. *ACS Appl. Mater. Interfaces* **2020**, *12*, 38266–38274. [CrossRef]
45. Barman, D.; Borah, J.; Deb, S.; Sarma, B.K. Design strategy for CuO-ZnO S-scheme heterojunction photocatalysts in the presence of plasmonic Ag and insights into photoexcited carrier generation and interfacial transfer in diverse structural configurations of the heterostructure system. *Colloids Surf. A Physicochem. Eng. Asp.* **2023**, *663*, 131077. [CrossRef]
46. Fang, J.; Fan, H.; Ma, Y.; Wang, Z.; Chang, Q. Surface defects control for ZnO nanorods synthesized by quenching and their anti-recombination in photocatalysis. *Appl. Surf. Sci.* **2015**, *332*, 47–54. [CrossRef]
47. Bao, C.; Chen, M.; Jin, X.; Hu, D.; Huang, Q. Efficient and stable photocatalytic reduction of aqueous hexavalent chromium ions by polyaniline surface-hybridized ZnO nanosheets. *J. Mol. Liq.* **2019**, *279*, 133–145. [CrossRef]
48. Hu, J.; Chen, C.; Yang, H.; Yang, F.; Qu, J.; Yang, X.; Sun, W.; Dai, L.; Li, C.M. Tailoring well-ordered, highly crystalline carbon nitride nanoarrays via molecular engineering for efficient photosynthesis of H_2O_2. *Appl. Catal. B Environ.* **2022**, *317*, 121723. [CrossRef]
49. Yin, H.; Cao, Y.; Fan, T.; Zhang, M.; Yao, J.; Li, P.; Chen, S.; Liu, X. In situ synthesis of Ag_3PO_4/C_3N_5 Z-scheme heterojunctions with enhanced visible-light-responsive photocatalytic performance for antibiotics removal. *Sci. Total Environ.* **2021**, *754*, 141926. [CrossRef] [PubMed]
50. Ai, Y.; Hu, J.; Xiong, X.; Carabineiro, S.A.C.; Li, Y.; Sirotkin, N.; Agafonov, A.; Lv, K. Synergistic interfacial engineering of a S-scheme ZnO/In_2S_3 photocatalyst with S−O covalent bonds: A dual-functional advancement for tetracycline hydrochloride degradation and H2 evolution. *Appl. Catal. B Environ. Energy* **2024**, *353*, 124098. [CrossRef]
51. Xiong, J.; Li, X.; Huang, J.; Gao, X.; Chen, Z.; Liu, J.; Li, H.; Kang, B.; Yao, W.; Zhu, Y. CN/rGO@BPQDs high-low junctions with stretching spatial charge separation ability for photocatalytic degradation and H_2O_2 production. *Appl. Catal. B Environ.* **2020**, *266*, 118602. [CrossRef]
52. Nosaka, Y.; Nosaka, A.Y. Generation and Detection of Reactive Oxygen Species in Photocatalysis. *Chem. Rev.* **2017**, *117*, 11302–11336. [CrossRef] [PubMed]

Disclaimer/Publisher's Note: The statements, opinions and data contained in all publications are solely those of the individual author(s) and contributor(s) and not of MDPI and/or the editor(s). MDPI and/or the editor(s) disclaim responsibility for any injury to people or property resulting from any ideas, methods, instructions or products referred to in the content.